Solvent-Free Synthesis of CuO/HKUST-1 Composite and Its Photocatalytic Application

Ming Jin,[†] Xuefeng Qian,[‡] Junkuo Gao,[*,‡] Jihua Chen,[§] Dale K. Hensley,[§] Hoi Chun Ho,[§] Rebecca J. Percoco,[∥] Christopher M. Ritzi,[∥] and Yanfeng Yue[*,∥]

[†]College of Chemistry and Chemical Engineering, Qufu Normal University, Qufu, Shandong 273165, P. R. China

[‡]Institute of Fiber Based New Energy Materials, The Key Laboratory of Advanced Textile Materials and Manufacturing Technology of Ministry of Education, College of Materials and Textiles, Zhejiang Sci-Tech University, Hangzhou, Zhejiang 310018, P. R. China

[§]Center for Nanophase Materials Sciences, Oak Ridge National Laboratory, Oak Ridge, Tennessee 37831, United States

[∥]Department of Biology, Geology, and Physical Sciences, Sul Ross State University, Alpine, Texas 79832, United States

Abstract: A metal−organic framework (MOF) is one kind of crystalline microporous material and is increasingly used as a host of catalytically active guests. Nanostructured materials supported on MOFs have presented enhanced catalytic activity and stability. Templates or several steps are essential to the synthesis of MOF composites. Simple and effective MOF synthesis methods are still challenging. Nanosized copper oxide particles in MOF composites, described as nanosized CuO@HKUST-1, were prepared by a facile solvent-free reaction. These series of CuO@HKUST-1 composites exhibited excellent photocatalytic activity for production of hydrogen and methylene blue (MB) degradation under visible light. This synthesis method provides an effective way to fabricate MOF-related nanocomposite catalysts.

Introduction

The metal−organic framework (MOF) is a new kind of crystalline microporous solid in which metal ions or clusters and organic ligands are assembled into a periodic framework.[1,2] MOFs have rigid three-dimensional topology and a large internal surface area. These structures make the MOF promising for various applications, such as gas storage,[3,4] gas purification,[5−7] heterogeneous catalysis,[8−10] and chemical sensing.[11,12]

Recently, MOF composites, created by embedding nanosized particles in classical microporous skeletons, have become a topic of intense interest.[13,14] This increased interest is due to the fact that MOF composites frequently exhibit improved properties compared to those from a simple mixture of the different components. Significant efforts are therefore being undertaken to construct MOF composites with functional species confined in the microporous networks, such as nanosized metal particles or oxides.[15,16]

Until now, research studies about MOF-related composites with graphene oxide (GO),[17−19] Fe3O4,[20−22] ZnO,[23,24] precious metal nanoparticles,[25−27] and alumina[28,29] or silica[30,31] have been reported. For instance, GO/HKUST-1 (HKUST-1 = $[Cu_3(BTC)_2]$, where BTC is 1,3,5-benzenetricarboxylate) nanocomposites exhibited an enhanced hydrogen absorption.[32] Bandosz and co-workers reported that the GO/MOF-5 composite also showed an increased ammonia adsorption compared to that of the parent MOF-5.[33] However, the synthesis of most of the MOF-related nanocomposites needs template agents or multistep preparations, thus adding to preparation time and costs. Therefore, facile methods to synthesize MOF-related nanocomposites are in great demand, such as the in situ one-pot synthesis from the MOF precursors and functional additives. This is especially true for the large scale production of MOF-related nanocomposites for gas separation and heterogeneous catalysis. Furthermore, the fabrication of

MOF-related nanocomposites with a controlled morphology and optimal synergistic effects of each component remains a big challenge in the functional materials community.[34–36]

Catalytic hydrogen evolution from water is a green and promising solution for the problem of climate change and environmental remediation. Meanwhile, the clean hydrogen production will help satisfy the ever-growing demands of fossil fuel energy in the next decades.[37–39] Among the discovered hydrogen evolution methods, photocatalytic water splitting is one of the most practical methods because of its low operating cost and almost unlimited solar radiation energy. However, photocatalytic hydrogen evolution from water driven by a highly efficient photocatalyst still remains a big challenge. Currently, most of the catalysts are semiconductors, among which metal oxide has been studied extensively, due to its low cost and high efficiency.[40–43] For photocatalytic water splitting, photons are absorbed by the metal oxide semiconductors, where the water splits into hydrogen and oxygen.[44,45] The photocatalytic performance of a catalyst is dominated by the number of photogenerated excitons which are easy to recombine. Both the generation and recombination of the excitons are closely related to the morphology and composition of the catalysts. Due to high surface areas and short diffusion distances compared to the bulk counterparts, nanoporous hybrid structured catalysts can benefit the molecule transfer. Thus, a promising approach to develop a solar sensitive photocatalyst is to introduce catalytically active semiconductors into the nanoporous lattice, in which porous lattices absorb light in the visible range.[46,47] Meanwhile, as a beneficial result of making nanocomposite porous catalysts, a delay in the recombination of the photogenerated charges can be provided. Therefore, the holes and electrons can be effectively separated in the different component layers resulting in a higher photoefficiency. It has been demonstrated that the nanostructures of the composite materials are favorable for improving the photoefficiency, as a result of offering large

surface areas and more exposed reactive sites for water splitting reactions. Our previous work also has investigated mesoporous metal sulfides with improved photocatalytic efficiency under visible light.[48] Therefore, it is a promising method to fabricate photocatalysts with nanosized metal oxide particles and porous frameworks as supports.

In the present paper, to the best of our knowledge, for the first time CuO@HKUST-1 composites were prepared using a solvent-free method from a nanosized CuO precursor. CuO@HKUST-1 nanocomposites can be easily prepared on a large scale based on this one-pot reaction. An investigation of photocatalytic performance by the composite on hydrogen evolution using visible light was then completed. These CuO@HKUST-1 nanocomposites exhibited an excellent photocatalytic hydrogen production performance due to the photocatalytic properties supplied by the trapped nanosized CuO, high surface areas, and accessible microporous channels for fast molecule diffusion. For extensive catalytic applications, an investigation of photocatalytic degradation by these nanocomposites on methylene blue under visible light was also carried out.

Experimental Section

Materials. Materials including copper(II) oxide (<50 nm, FW 79.55), 1,3,5-benzenetricarboxylatic acid (H3BTC, FW 210.14), dimethylformamide (DMF), and ethanol were all received from Aldrich and were used without any further purification.

Synthesis of MOF-Related Nanocomposite. For the CuO@HKUST-1-20/12 composite, copper(II) oxide (0.80 g, 10 mmol) and H_3BTC (1.26 g, 6 mmol) were ground together for 30 min before they were placed into an autoclave. The autoclave was closed tightly, heated to 180 °C in an oven, and kept at that temperature for 96 h. After the autoclave cooled down to room

temperature, the resulting products were washed with ethanol three times and dried under vacuum at 60 °C for 12 h. The product was named CuO@HKUST-1-20/12, in which 20/12 stands for the ratio of CuO and H_3BTC precursors being 20:12. The CuO@HKUST-1-20/3 composite was also synthesized by mixing the reactants directly, following a procedure similar to that for CuO@HKUST-1-20/12, with the starting CuO/H_3BTC ratio being 20/3 (0.80 g CuO and 0.31 g H_3BTC).

Material Characterizations. The crystallinity and the phase purity of the CuO@HKUST-1 nanocomposites were characterized by powder X-ray diffraction (XRD) analysis. The powder XRD diffractograms were obtained using a Bruker D2 Phaser X-ray powder diffractometer equipped with Cu Kα radiation (λ = 1.5406 Å). The morphologies of the nanocomposites were characterized via transmission electron microscopy (TEM) and scanning electron microscopy (SEM) on a Hitachi HD2000 STEM microscope operating at 200 kV. The samples for image analysis were prepared by drop casting: one drop of the sample dispersion in ethanol was carefully loaded onto a copper grid and allowed to dry at room temperature before being subjected to the electron image collection. The permanent porosity and surface areas of the CuO@HKUST-1 nanocomposites were determined on a Micromeritics ASAP 2020. About 100 mg of as-made product was activated for 6 h at 150 °C under vacuum and subsequently loaded for nitrogen adsorption analysis at 77 K.

Photocatalytic Hydrogen Evolution Measurements. The photocatalytic hydrogen evolution was carried out in a Labsolar-IIIAG photocatalytic system (Beijing Perfectlight Technology Co., Ltd.) using a 300 W Xe lamp equipped with a UV cutoff filter (λ > 420 nm). The details follow: 50 mg of CuO@HKUST-1 nanocomposite was dispersed into a mixture solution containing 88

mL of acetonitrile, 10 mL of triethanolamine, and 2 mL of deionized water. The reaction temperature was set as 1 °C, and hydrogen gas was measured every 1 h.

The photocatalytic methylene blue (MB) degradation was carried out at room temperature under visible light. The details follow: 12.5 mg of CuO@HKUST-1 nanocomposite was dispersed in 15 mL of aqueous solution of MB (55 mg L^{-1}). Under dark conditions, the suspension was stirred for 30 min to achieve adsorption equilibrium. Then, 0.1 mL of hydrogen peroxide (H_2O_2, 30%) was added into the above solution. The photocatalytic MB degradation was conducted by irradiating the suspension with a 300 W xenon lamp coupled with a UV cutoff filter ($\lambda > 400$ nm) while stirring. Every 30 min the samples (1 mL) were withdrawn from the reactor; the powder was suspended by centrifugation and analyzed by ultraviolet−visible (UV−vis) spectroscopy. The efficiency of dye degradation was obtained by C/C_0, where C is the concentration of undecomposed MB and C_0 is the initial concentration of MB. The cycle test of photocatalytic MB degradation was carried out by centrifugation of the reaction solution, and the catalyst was reused three times. In order to understand the photocatalysis mechanism, benzoquinone (BQ), isopropyl alcohol (IPA), and EDTA-2Na were separately added as scavengers for hydroxyl radicals ($^{\bullet}OH$), superoxide radicals ($^{\bullet}O2^{-}$), and holes (h^{+}) to the MB solution before the photocatalyst was added. The concentration of IPA, BQ, and EDTA-2Na in MB solution was 1 mM, while the other conditions remained the same as those used for the photocatalytic MB degradation.

Electrochemical Measurements. For the working electrode preparation, 5 mg of ground sample was ultrasonically dispersed for 30 min in a solution of 0.5 mL methanol and 30 μL Nafion solution. After 30 min of sonication, a fluorine-doped tin oxide (FTO) glass with a fixed area of 0.5 cm^2 was coated by 10 μL of the obtained slurry. The working electrode was dried in air at 60

°C for 10 min. A 0.5 M Na_2SO_4 solution was employed as supporting electrolyte. The Mott−Schottky curves were obtained in the dark at a frequency of 10 Hz. A three-electrode cell was employed for the measurements with a Pt plate, and a Ag/AgCl electrode was used as counter electrode and reference electrode, respectively.

Results and Discussion

Mechanism of the Preparation of CuO@HKUST-1 Nanocomposite. The synthesis of CuO@HKUST-1 nanocomposites based on a conventional solid-state reaction requires a mechanical mixing of solid metal oxide precursor and organic ligand. In detail, the CuO@HKUST-1 nanocomposite was synthesized by an in situ growth of MOF nanocrystal on the CuO nanosized precursors (Scheme 1). There is a strong interaction between the ligand and CuO nanoparticles. As a consequence, the nucleation and growth of the MOF crystals proceeded and resulted in CuO nanoparticles trapped in the MOF lattice. First, the basic CuO nanoparticles deprotonated the acidic H_3BTC ligand and give out Cu(II) ions. The ligands further coordinate with the Cu(II) ions on the surfaces of CuO particles resulting in HKUST-1. Then, the CuO particles continue to release the Cu(II) ions and more HKUST-1 formes and CuO particles gradually decrease their size and trapped in the HKUST-1 lattice. Finally, CuO@HKUST-1 nanocomposites with different CuO sizes can be obtained by controlling the reactant ratios. This facile solvent-free synthetic method obviously would reduce pollution and lower costs. Additionally, the final products from this solvent-free method turned out to be different from those obtained in wet reactions. This is because of specific spatial orientation or crystal growth under a solvent-free condition, which will provide excellent opportunities to achieve nanocomposites with controlled compatibility between component materials.

Structural and Morphology Properties of CuO@HKUST-1 Nanocomposites. In a comparison of the powder X-ray diffraction patterns of the CuO@HKUST-1 with that of CuO precursor and pristine HKUST-1, it can be confirmed that the composites have the HKUST-1 crystal structure (Figure 1a). Furthermore, XRD analyses also verified the existence of the CuO phase in the nanocomposites. The adsorption properties of the composites have been determined by N_2 adsorption measurements (Figure 1b). Both CuO@HKUST-1 nanocomposites exhibit type I isotherms, which is typical for microporous materials. Compared to CuO@HKUST-1-20/12, the lower gas uptake of CuO@HKUST-1-20/3 indicates more nonporous CuO in the resultant product. The Brunauer−Emmett−Teller (BET) surface areas of CuO@HKUST-1-20/12 and CuO@HKUST-1-20/3 are 296 and 29 m^2/g, respectively (Figure 1b). The nitrogen adsorption isotherm of HKUST-1 is shown in Figure S10. The BET surface of pure HKUST-1 is 951 m^2/g, which is substantially higher than that of the CuO@HKUST-1 nanocomposite, indicating that the incorporation of CuO into the HKUST-1 network dramatically decreased the surface area. The distribution of the pore size was calculated by using the Horvath−Kawazoe (H-K) method as shown in Figures S11 and S12.

The FT-IR spectra of the nanocomposites, CuO precursor, and pure HKUST-1 are shown in Figure 2. The adsorption band at 1508−1623 cm^{-1} corresponds to the asymmetric stretching of the carboxylate groups in HKUST-1. The symmetric stretching of the carboxylate groups in HKUST-1 is also observed at 1384 and 1405 cm^{-1}. The out-of-plane vibrations of ligands in HKUST-1 correspond to several bands in the region 1300−600 cm^{-1}.[49] The absorption band around 500 cm^{-1} is the specific vibration of the Cu−O bonds.[50] The FT-IR spectra indicate the CuO particles and HKUST-1 were all preserved in the composite products.

The content of HKUST-1 in the composites is quantified by thermogravimetric analysis as shown in Figures S7−S9. The total mass is obtained after the adsorbed water molecules of the composites have completely been removed at about 200 °C. The content of HKUST-1 in the composites is quantified by the following equation:

$$A = \frac{M_1 - M_2}{M_1} \div \frac{M_{01} - M_{02}}{M_{01}} \times 100\%$$

Here, A is the content of HKUST-1. M_1 is the mass of composites, and M_2 is the mass of the composites decomposition products at about 340 °C. M_{01} is the mass of the pristine HKUST-1, and M_{02} is the mass of the pristine HKUST-1 total decomposition products at 340 °C. After being calculated, the contents of HKUST-1 in CuO@HKUST-1-20/3 and CuO@HKUST-1-20/12 are 7.9% and 30.5%, respectively.

The morphology and the CuO particle size of the nanocomposites were characterized using SEM and TEM, as seen in Figure 3. The CuO@HKUST-1-20/12 has polyhedron morphology with sharp facets, with sizes ranging from 300 to 500 nm (Figure 2a). The CuO nanoparticles in a range of 5−40 nm are embedded in HKUST-1 crystal particles (Figure 2b), indicating that the precursor CuO was partially consumed.

Interestingly, the particle size of CuO can be tuned by adjusting the ratio of the reactants. When the molar ratio of CuO and H_3BTC was changed from 20:12 to 20:3, larger CuO nanoparticles were trapped in the MOF network (Figure 3). These observations support the proposed mechanism that CuO nanoparticles initially deprotonate the ligand on the interfaces and serve as metal resources for the formation of the MOF shell. The formation of CuO@HKUST-1 under solvent-free conditions is quite different from the homogeneous nucleation process from soluble Cu(II) salts in wet reactions.

Photocatalytic Hydrogen Evolution and MB Degradation. The procedure of the photocatalytic hydrogen evolution is described here: 50 mg of CuO@HKUST-1 nanocomposite was dispersed into a mixture solution containing 88 mL of acetonitrile, 10 mL of triethanolamine, and 2 mL of deionized water. The diffuse reflectance spectra of the CuO@HKUST-1 nanocomposites are similar and show a broad range of absorption in the visible light region extending to 1100 nm. The intensity from the CuO@HKUST-1 nanocomposites is higher than those from CuO and HKUST-1, indicating that the nanocomposites possess a good light absorption performance (Figure 4a). Photocatalytic activities of CuO@HKUST-1 nanocomposites were examined for photocatalytic hydrogen evolution and MB degradation under visible light irradiation.

For comparison, the photocatalytic activities of the pristine HKUST-1 and the commercial CuO nanoparticles were also investigated. The hydrogen evolution rates of HKUST-1 and CuO are 70 and 510 μmol g^{-1} h^{-1}, respectively (Figure 4b). The CuO@HKUST-1-20/12 shows the highest photocatalytic activity with a H_2 evolution rate of 667 μmol g^{-1} h^{-1}, and the H_2 evolution rate of CuO@HKUST-1-20/3 is 620 μmol g^{-1} h^{-1}. The H_2 evolution rate of CuO@HKUST-1-20/12 is 9.5 and 1.3 times those of HKUST-1 and CuO, respectively, indicating that the approach described in this paper can efficiently improve the photocatalytic activity. Furthermore, CuO@HKUST-1-20/12 shows high photocatalytic stability and almost no catalytic efficiency decay even after recycling three times (Figure 5).

As shown in Figure 4c, about 75% and 80% of MB molecules were degraded within 180 min for the pristine HKUST-1 and commercial CuO nanoparticles, whereas 98% MB degradation was achieved in the presence of the CuO@HKUST-1 composite. It is necessary to note that the CuO@HKUST-1 composites presented equal performance on the degradation of MB, which is consistent with their similar diffuse reflectance spectra. In consideration of their

differences in BET surface area and CuO nanoparticles size, it is speculated that the pore sizes of CuO@HKUST-1 nanocomposites were too small to effectively transfer large dye molecules such as the MB molecule. The small pore size of CuO@HKUST-1 nanocomposites would have mitigated the photocatalytic activity of CuO@HKUST-1-20/12. To investigate the photodegradation mechanism, isopropanol (IPA) is employed as a scavenger for hydroxyl radical ($^{\bullet}OH$), EDTA disodium salt (EDTA-2Na) for photogenerated holes (h^+), and benzoquinone (BQ) for superoxide radical ($^{\bullet}O2^-$). The results showed the influence of the three scavengers on the solution (Figure S1). The hydroxyl radical ($^{\bullet}OH$) and photogenerated holes (h^+) were the two main active species in this CuO@HKUST-1 photocatalytic system in view of the inhibition order (EDTA-2Na > IPA > BQ) (Figure 6).

The Mott−Schottky characterizations were also conducted to further reveal the flat-band potential of HKUST-1 and CuO. The flat-band potentials (V_{fb}) of CuO and HKUST-1 are about 0.68 and −0.05 V vs Ag/AgCl (0.26 V vs NHE) shown respectively in Figures S2 and S3. The band gap values of CuO and HKUST-1 are about 1.46 and 2.62 eV (vs NHE), respectively, which were estimated using the related curve of $(\alpha h\nu)^2$ versus photon energy (Figures S4 and S5), while the valence bands (VB) of CuO and HKUST-1 are 2.14 and 2.57 eV (vs NHE), respectively. When the photocatalyst is irradiated under visible light, the excited electrons transfer from the CB of HKUST-1 to that of the CuO for evolving water to hydrogen (Figure 7). The sacrificial electron donor was oxidized by the photogenerated holes in the VB of HKUST-1 rapidly, which promoted photocatalytic processes. For the degradation of MB, when the excited electrons transfer from the CB of HKUST-1 to that of CuO, $^{\bullet}OH$ radicals are produced as the consequence of the capture of H_2O_2. The holes in the VB of HKUST-1 transferred from the CB of CuO can oxidize H_2O to give $^{\bullet}OH$ and to further oxidize MB directly.

Conclusion

In summary, CuO@HKUST-1 nanocomposites were successfully fabricated by a facile solvent-free method based on a one-pot reaction. The surface morphology, porosity, and particle size of trapped CuO of the CuO@HKUST-1 nanocomposites can be simply adjusted by tuning the ratio of the reactants. Compared to the pristine HKUST-1 and the commercial CuO nanoparticles, the CuO@HKUST-1 nanocomposites showed an improved photocatalytic activity for the hydrogen evolution under visible irradiation. Hence, this synthesis method opens a new route to obtain various other MOF-based nanocomposites in a high yield which can be used as heterogeneous catalysts, chemical sensors, and electrochemical energy storage devices.

Acknowledgments

Electron microscopy (J.C., H.C.H., and D.K.H.) experiments were conducted at the Center for Nanophase Materials Sciences, which is a DOE Office of Science User Facility.

References

(1) Shekhah, O.; Liu, J.; Fischer, R. A.; Wöll, C. MOF thin films: existing and future applications. Chem. Soc. Rev. 2011, 40, 1081−1106.

(2) Stavila, V.; Talin, A. A.; Allendorf, M. D. MOF-based electronic and opto-electronic devices. Chem. Soc. Rev. 2014, 43, 5994−6010.

(3) Sumida, K.; Rogow, D. L.; Mason, J. A.; McDonald, T. M.; Bloch, E. D.; Herm, Z. R.; Bae, T.; Long, J. R. Carbon dioxide capture in metal-organic frameworks. Chem. Rev. 2012, 112, 724−781.

(4) Zou, F.; Hu, X.; Li, Z.; Qie, L.; Hu, C.; Zeng, R.; Jiang, Y.; Huang, Y. MOF-derived porous ZnO/$ZnFe_2O_4$/C octahedra with hollow interiors for high-rate lithium-ion batteries. Adv. Mater. 2014, 26, 6622−6628.

(5) An, J.; Rosi, N. L. Tuning MOF CO_2 adsorption properties via cation exchange. J. Am. Chem. Soc. 2010, 132, 5578−5579.

(6) Saha, D.; Bao, Z.; Jia, F.; Deng, S. Adsorption of CO_2, CH_4, N_2O, and N_2 on MOF-5, MOF-177, and zeolite 5A. Environ. Sci. Technol. 2010, 44, 1820−1826.

(7) Yang, D.; Cho, H.; Kim, J.; Yang, S.; Ahn, W. CO_2 capture and conversion using Mg-MOF-74 prepared by a sonochemical method. Energy Environ. Sci. 2012, 5, 6465−6473.

(8) Juan-Alcañiz, J.; Ramos-Fernandez, E. V.; Lafont, U.; Gascon, J.; Kapteijn, F. Building MOF bottles around phosphotungstic acid ships: one-pot synthesis of bi-functional polyoxometalate-MIL-101 catalysts. J. Catal. 2010, 269, 229−241.

(9) Yoon, M.; Srirambalaji, R.; Kim, K. Homochiral metal-organic frameworks for asymmetric heterogeneous catalysis. Chem. Rev. 2012, 112, 1196−1231.

(10) Das, M. C.; Xu, H.; Wang, Z.; Srinivas, G.; Zhou, W.; Yue, Y.-F.; Nesterov, V. N.; Qian, G.; Chen, B. A Zn_4O-containing doubly interpenetrated porous metal−organic framework for photocatalytic decomposition of methyl orange. Chem. Commun. 2011, 47, 11715−11717.

(11) Hao, Z. M.; Song, X. Z.; Zhu, M.; Meng, X.; Zhao, S. N.; Su, S. Q.; Yang, W. T.; Song, S. Y.; Zhang, H. J. One-dimensional channel-structured Eu-MOF for sensing small organic molecules and Cu^{2+} ion. J. Mater. Chem. A 2013, 1, 11043−11050.

(12) Wang, J.-H.; Li, M.; Li, D. A dynamic, luminescent and entangled MOF as a qualitative sensor for volatile organic solvents and a quantitative monitor for acetonitrile vapour. Chem. Sci. 2013, 4, 1793−1801.

(13) Moon, H. R.; Lim, D. W.; Suh, M. P. Fabrication of metal nanoparticles in metal−organic frameworks. Chem. Soc. Rev. 2013, 42, 1807−1824.

(14) Cui, Y.; Song, R.; Yu, J.; Liu, M.; Wang, Z.; Wu, C.; Yang, Y.; Wang, Z.; Chen, B.; Qian, G. Dual-emitting MOF⊃dye composite for ratiometric temperature sensing. Adv. Mater. 2015, 27, 1420−1425.

(15) Lu, G.; Li, S.; Guo, Z.; Farha, O. K.; Hauser, B. G.; Qi, X.; Wang, Y.; Wang, X.; Han, S.; Liu, X.; DuChene, J. S.; Zhang, H.; Zhang, Q.; Chen, X.; Ma, J.; Loo, S. C. J.; Wei, W. D.; Yang, Y.; Hupp, J. T.; Huo, F. Imparting functionality to a metal−organic framework material by controlled nanoparticle encapsulation. Nat. Chem. 2012, 4, 310−316.

(16) Liu, Y.; Tang, Z. Multifunctional nanoparticle@MOF core−shell nanostructure. Adv. Mater. 2013, 25, 5819−5825.

(17) Jahan, M.; Bao, Q.; Loh, K. P. Electrocatalytically active graphene-porphyrin MOF composite for oxygen reduction reaction. J. Am. Chem. Soc. 2012, 134, 6707−6713.

(18) Petit, C.; Bandosz, T. J. Exploring the coordination chemistry of MOF−graphite oxide composites and their applications as adsorbents. Dalton Trans. 2012, 41, 4027−4035.

(19) Mehek, R.; Iqbal, N.; Noor, T.; Nasir, H.; Mehmood, Y.; Ahmed, S. Novel Co-MOF/graphene oxide electrocatalyst for methanol oxidation. Electrochim. Acta 2017, 255, 195−204.

(20) Ke, F.; Qiu, L.; Yuan, Y.; Jiang, X.; Zhu, J.-F. Fe_3O_4@MOF core−shell magnetic microspheres with a designable metal−organic framework shell. J. Mater. Chem. 2012, 22, 9497−9500.

(21) Yang, Y.; Xia, F.; Yang, Y.; Gong, B.; Xie, A.; et al. Litchi-like Fe_3O_4@Fe-MOF capped with HAp gatekeepers for pH-triggered drug release and anticancer effect. J. Mater. Chem. B 2017, 5, 8600−8606.

(22) Li, J.; Wang, J.; Ling, Y.; Chen, Z.; Gao, M.; Zhang, X.; Zhou, Y. Unprecedented highly efficient capture of glycopeptides by Fe_3O_4@Mg-MOF-74 core−shell nanoparticles. Chem. Commun. 2017, 53, 4018−4021.

(23) Yue, Y.; Qiao, Z.; Li, X.; Binder, A. J.; Formo, E.; Pan, Z.; Tian, C.; Bi, Z.; Dai, S. Nanostructured zeolitic imidazolate frameworks derived from nanosized zinc oxide precursors. Cryst. Growth Des. 2013, 13, 1002−1005.

(24) Li, W.; Wu, X.; Han, N.; Chen, J.; Qian, X.; Deng, Y.; Tang, W.; Chen, Y. MOF-derived hierarchical hollow ZnO nanocages with enhanced low-concentration VOCs gas-sensing performance. Sens. Actuators, B 2016, 225, 158−166.

(25) Zhao, M.; Deng, K.; He, L.; Liu, Y.; Li, G.; Zhao, H.; Tang, Z. Core-shell palladium nanoparticle@metal-organic frameworks as multifunctional catalysts for cascade reactions. J. Am. Chem. Soc. 2014, 136, 1738−1741.

(26) Zhou, J.; Wang, P.; Wang, C.; Goh, Y. T.; Fang, Z.; Messersmith, P. B.; Duan, H. Versatile core-shell nanoparticle@metal-organic framework nanohybrids: Exploiting mussel-inspired polydopamine for tailored structural integration. ACS Nano 2015, 9, 6951−6960.

(27) Yang, Q.; Liu, W.; Wang, B.; Zhang, W.; Zeng, X.; Zhang, C.; Qin, Y.; Sun, X.; Wu, T.; Liu, J.; Huo, F.; Lu, J. Regulating the spatial distribution of metal nanoparticles within metal-organic frameworks to enhance catalytic efficiency. Nat. Commun. 2017, 8, 14429.

(28) Xu, X. Y.; Yan, B. Novel photofunctional hybrid materials (alumina and titania) functionalized with both MOF and lanthanide complexes through coordination bonds. RSC Adv. 2014, 4, 38761−38768.

(29) Xie, Z.; Li, T.; Rosi, N. L.; Carreon, M. A. Alumina-supported cobalt−adeninate MOF membranes for CO_2/CH_4 separation. J. Mater. Chem. A 2014, 2, 1239−1241.

(30) Gascon, J.; Aguado, S.; Kapteijn, F. Manufacture of dense coatings of $Cu_3(BTC)_2$ (HKUST-1) on α-alumina. Microporous Mesoporous Mater. 2008, 113, 132−138.

(31) Han, T.; Li, C.; Guo, X.; Huang, H.; Liu, D.; Zhong, C. In-situ synthesis of SiO_2@MOF composites for high-efficiency removal of aniline from aqueous solution. Appl. Surf. Sci. 2016, 390, 506−515.

(32) Petit, C.; Burress, J.; Bandosz, T. J. The synthesis and characterization of copper-based metal−organic framework/graphite oxide composites. Carbon 2011, 49, 563−572.

(33) Petit, C.; Bandosz, T. J. Enhanced adsorption of ammonia on metal-organic framework/graphite oxide composites: Analysis of surface interactions. Adv. Funct. Mater. 2010, 20, 111−118.

(34) Dhakshinamoorthy, A.; Asiri, A. M.; García, H. Metal−organic framework (MOF) compounds: photocatalysts for redox reactions and solar fuel production. Angew. Chem., Int. Ed. 2016, 55, 5414−5445.

(35) Tan, P.; Xie, X.-Y.; Liu, X.-Q.; Pan, T.; Gu, C.; Chen, P.-F.; Zhou, J.-Y.; Pan, Y.; Sun, L.-B. Fabrication of magnetically responsive HKUST-1/Fe_3O_4 composites by dry gel conversion for deep desulfurization and denitrogenation. J. Hazard. Mater. 2017, 321, 344−352.

(36) Li, Y.-X.; Ji, Y.-N.; Jin, M.-M.; Qi, S.-C.; Li, S.-S.; Xue, D.-M.; Yue, M. B.; Liu, X.-Q.; Sun, L.-B. Controlled construction of Cu(I) sites within confined spaces via host−guest redox: highly efficient adsorbents for selective CO adsorption. ACS Appl. Mater. Interfaces 2018, 10, 40044−40053.

(37) Steinfeld, A. Solar hydrogen production via a two-step water-splitting thermochemical cycle based on Zn/ZnO redox reactions. Int. J. Hydrogen Energy 2002, 27, 611−619.

(38) van de Krol, R.; Liang, Y.; Schoonman, J. Solar hydrogen production with nanostructured metal oxides. J. Mater. Chem. 2008, 18, 2311−2320.

(39) Li, Z.; Luo, W.; Zhang, M.; Feng, J.; Zou, Z. Photoelectrochemical cells for solar hydrogen production: current state of promising photoelectrodes, methods to improve their properties, and outlook. Energy Environ. Sci. 2013, 6, 347−370.

(40) Hara, M.; Kondo, T.; Komoda, M.; Ikeda, S.; Kondo, J. N.; Domen, K.; Hara, M.; Shinohara, K.; Tanaka, A. Cu_2O as a photocatalyst for overall water splitting under visible light irradiation. Chem. Commun. 1998, 357−358.

(41) Maeda, K.; Takata, T.; Hara, M.; Saito, N.; Inoue, Y.; Kobayashi, H.; Domen, K. GaN: ZnO solid solution as a photocatalyst for visible-light-driven overall water splitting. J. Am. Chem. Soc. 2005, 127, 8286−8287.

(42) Kato, H.; Kudo, A. Visible-light-response and photocatalytic activities of TiO_2 and $SrTiO_3$ photocatalysts codoped with antimony and chromium. J. Phys. Chem. B 2002, 106, 5029−5034.

(43) Niishiro, R.; Kato, H.; Kudo, A. Nickel and either tantalum or niobium-codoped TiO_2 and $SrTiO_3$ photocatalysts with visible-light response for H2 or O2 evolution from aqueous solutions. Phys. Chem. Chem. Phys. 2005, 7, 2241−2245.

(44) Khemthong, P.; Photai, P.; Grisdanurak, N. Structural properties of CuO/TiO_2 nanorod in relation to their catalytic activity for simultaneous hydrogen production under solar light. Int. J. Hydrogen Energy 2013, 38, 15992−16001.

(45) Hou, H.; Shang, M.; Gao, F.; Wang, L.; Liu, Q.; Zheng, J.; Yang, Z.; Yang, W. Highly efficient photocatalytic hydrogen evolution in ternary hybrid TiO_2/CuO/Cu thoroughly mesoporous nanofibers. ACS Appl. Mater. Interfaces 2016, 8, 20128−20137.

(46) Bao, N.; Shen, L.; Takata, T.; Domen, K. Self-templated synthesis of nanoporous CdS nanostructures for highly efficient photocatalytic hydrogen production under visible light. Chem. Mater. 2008, 20, 110−117.

(47) Li, Y.; Chen, G.; Zhou, C.; Sun, J. A simple template-free synthesis of nanoporous ZnS-In_2S_3-Ag_2S solid solutions for highly efficient photocatalytic H_2 evolution under visible light. Chem. Commun. 2009, 2020−2022.

(48) Yue, Y.; Li, Y.; Bridges, C. A.; Rother, G.; Zhang, J.; Chen, J.; Hensley, D. K.; Kidder, M. K.; Richardson, B. C.; Parans Paranthaman, M.; Dai, S. Hierarchically superstructured metal sulfides: Facile perturbation-assisted nanofusion synthesis and visible light photocatalytic characterizations. ChemNanoMat 2016, 2, 1104−1110.

(49) Li, L.; Liu, X. L.; Geng, H. Y.; Hu, B.; Song, G. W.; Xu, Z. S. A MOF/graphite oxide hybrid (MOF: HKUST-1) material for the adsorption of methylene blue from aqueous solution. J. Mater. Chem. A 2013, 1, 10292−10299.

(50) Ardelean, I.; Cora, S.; Rusu, D. EPR and FT-IR spectroscopic studies of Bi_2O_3−B_2O_3−CuO glasses. Phys. B 2008, 403, 3682−3685.

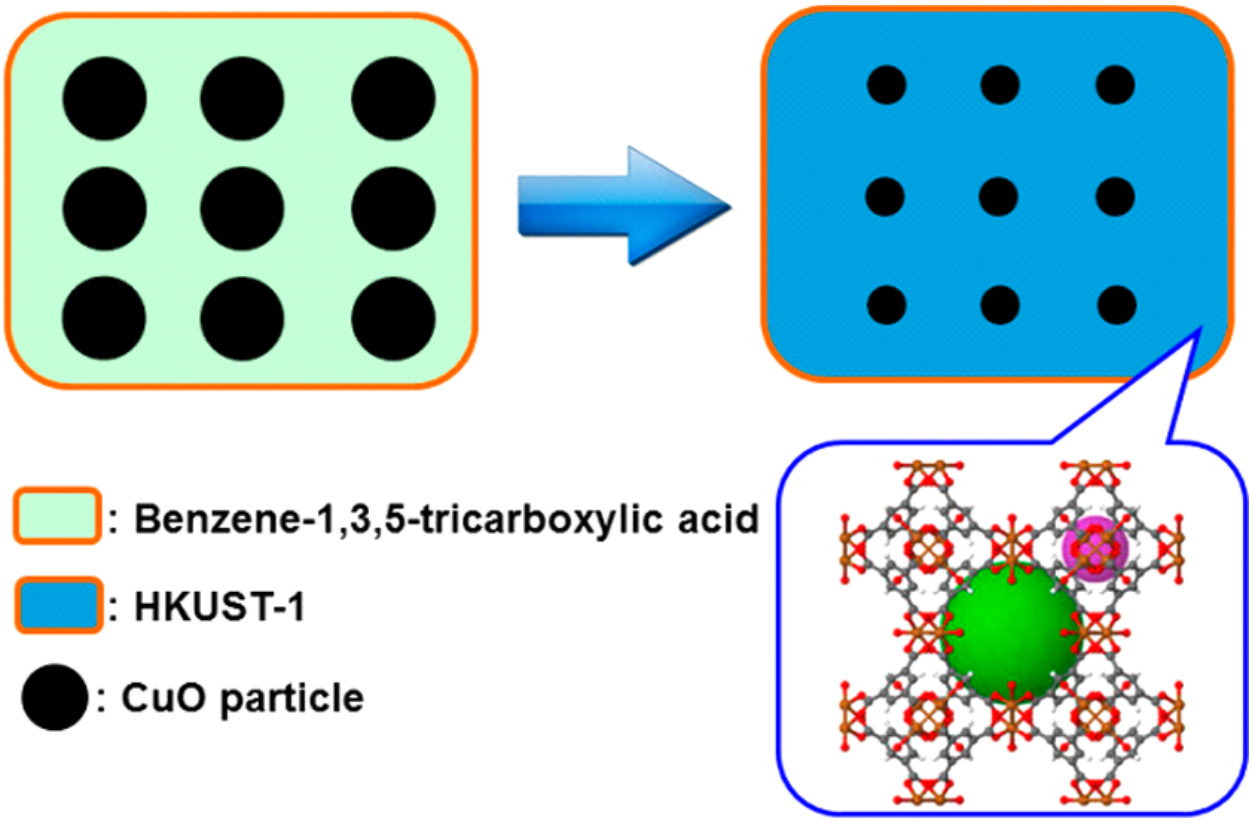

Scheme 1. Schematic Representation of the Solid-State Transformation from Nanosized Copper Oxide and Ligand BTC to CuO@HKUST-1 Composites

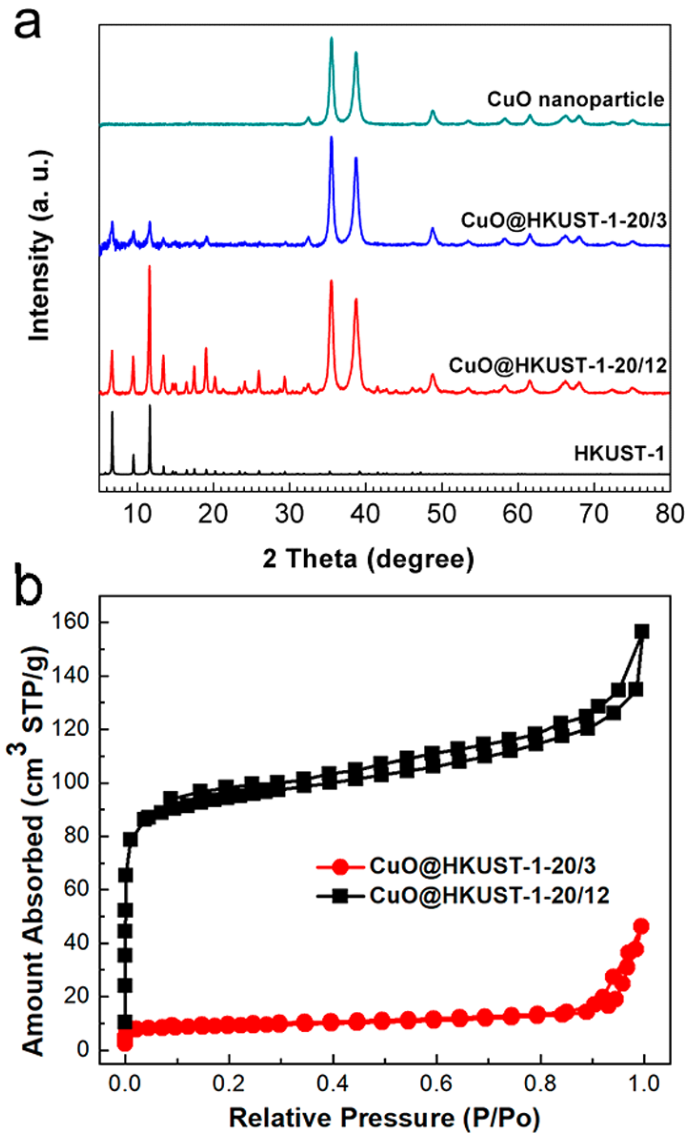

Figure 1. Powder XRD patterns of CuO@HKUST-1-20/12, CuO@HKUST-1-20/3, nanosized CuO precursor, and simulated XRD patterns from single crystal data of HKUST-1 (a) and nitrogen adsorption isotherms of CuO@HKUST-1-20/12, CuO@HKUST-1-20/3 (b).

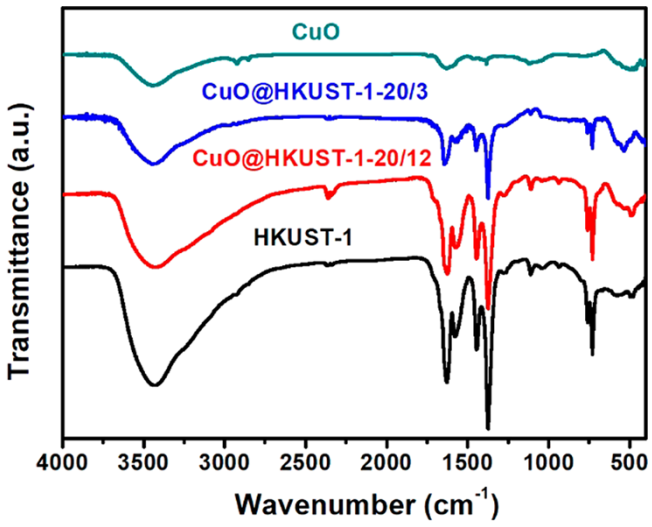

Figure 2. FT-IR spectra of CuO@HKUST-1-20/3, CuO@HKUST-1-20/12, and HKUST-1.

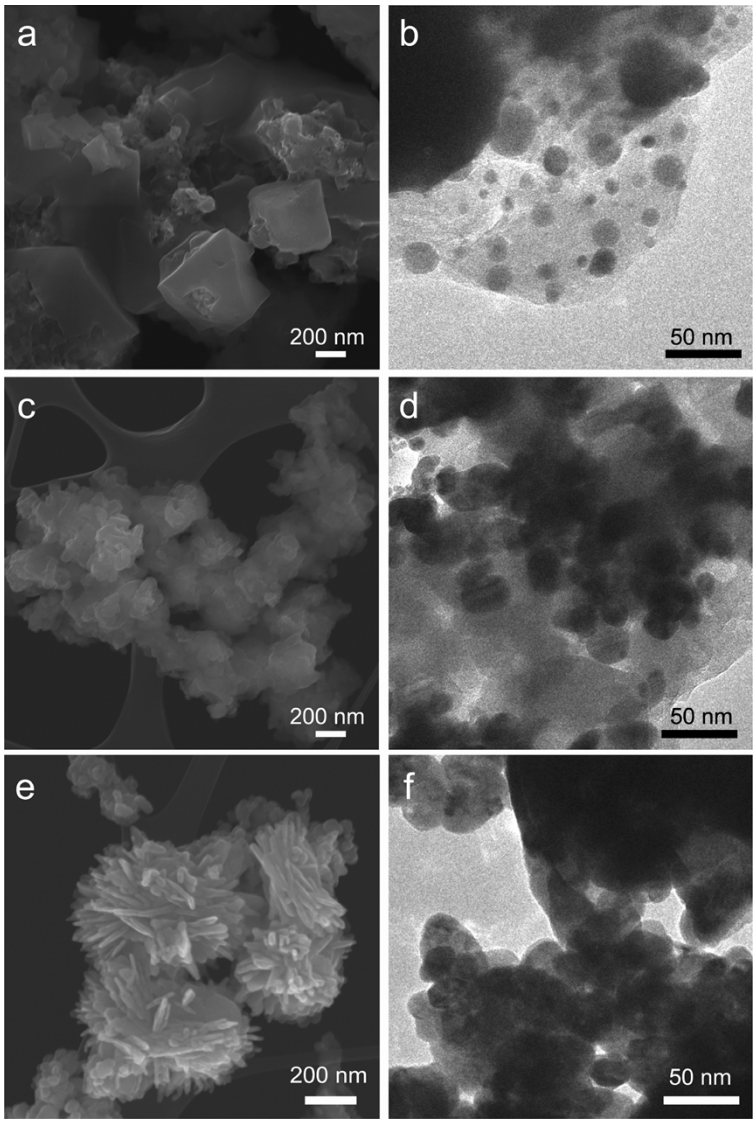

Figure 3. SEM images (a, c, e) and TEM images (b, d, f) for CuO@HKUST-1-20/12 (top), CuO@HKUST-1-20/3 (middle), and nanosized CuO precursor (bottom).

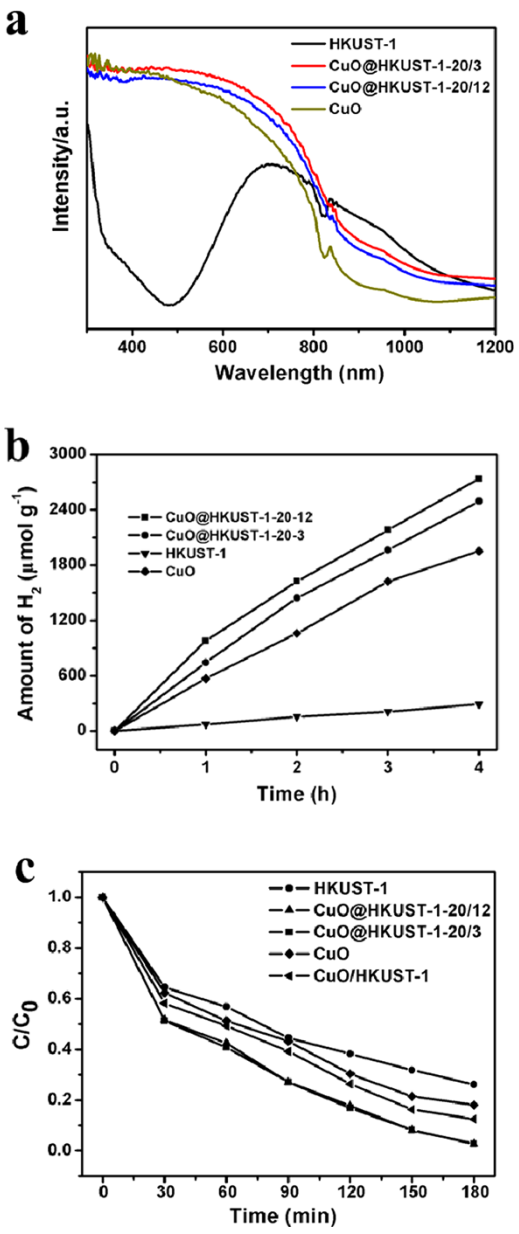

Figure 4. Solid-state UV−vis reflectance spectra (a) and H_2 evolution efficiency (b) of CuO, HKUST-1, CuO@HKUST-1-20/12, and CuO@HKUST-1-20/3. MB photodegradation of CuO, HKUST-1, CuO@HKUST-1-20/12, CuO@HKUST-1-20/3, and CuO/HKUST-1 (the mixture of CuO and HKUST-1) in the presence of H_2O_2 (c).

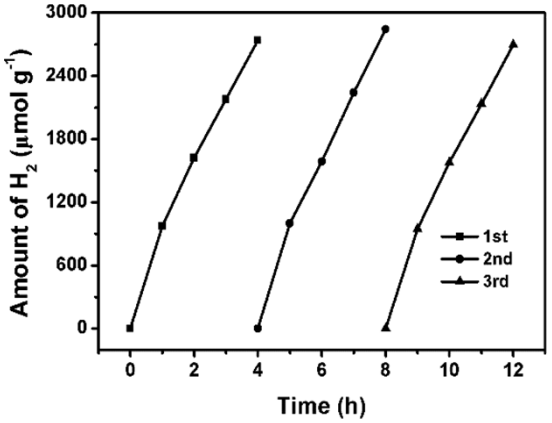

Figure 5. Stability test of CuO@HKUST-1-20/12.

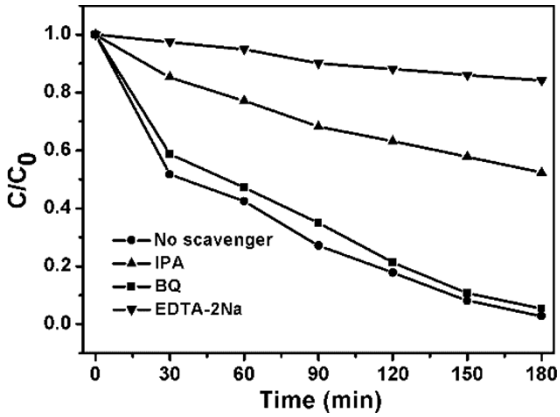

Figure 6. Photocatalytic activity of CuO@HKUST-1-20/12 to the degradation of MB with different scavengers.

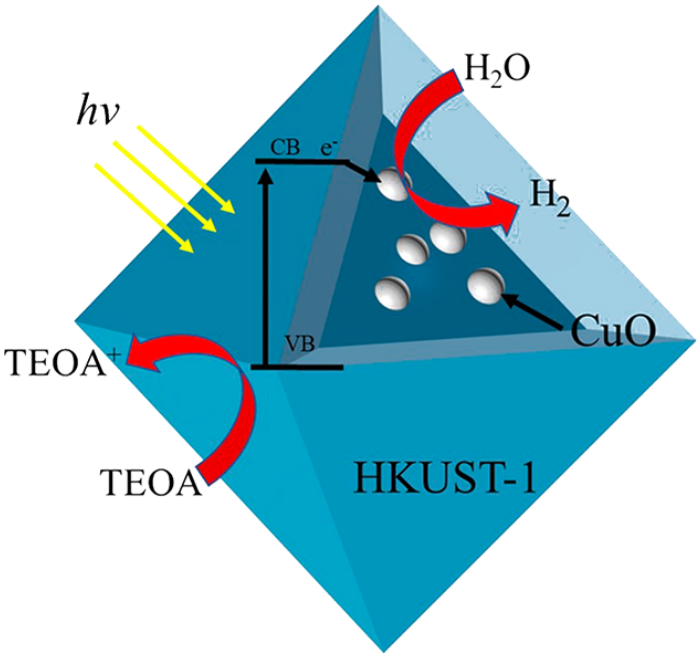

Figure 7. Schematic diagram of the photocatalytic H_2 generation over the HKUST-1/CuO heterojunctions.